ELSEVIER

Contents lists available at ScienceDirect

Journal of Nuclear Materials

journal homepage: www.elsevier.com/locate/jnucmat



Dispersoid stability in ion irradiated oxide-dispersion-strengthened alloy



Hyosim Kim ^a, Jonathan G. Gigax ^a, Tianyi Chen ^{a, b}, Shigeharu Ukai ^c, Frank A. Garner ^a, Lin Shao ^{a, *}

- ^a Department of Nuclear Engineering, Texas A&M University, TX, 77843, United States
- ^b Oak Ridge National Laboratory, Oak Ridge, TN, 37831, United States
- ^c Department of Material Science and Engineering, Hokkaido University: N13, W-8, Kita-ku, Sapporo, 060-0808, Japan

ARTICLE INFO

Article history: Received 8 December 2017 Received in revised form 9 July 2018 Accepted 9 July 2018 Available online 10 July 2018

ABSTRACT

The radiation response of oxide dispersoids in a Hf-doped oxide-dispersion-strengthened (ODS) alloy was studied by using 3.5 MeV Fe²⁺ self-ion irradiation at 475 °C. The size changes of coherent and incoherent dispersoids were studied as a function of depth. Although there was up to 2.6 times difference in local displacements-per-atom (dpa) rate at different characterization depths, the sizes of coherent and incoherent dispersoids did not show a noticeable dependence on dpa rate at depths up to the peak dpa position. In order to explain the experimental observations, the diffusion of solute atoms (dissolved from dispersoids) must take into consideration defect-assisted-diffusion mechanisms. A high dpa rate results in enhanced dispersoid dissolution. On the other hand, dispersoid recovery is increased due to defect-assisted diffusion. Therefore, the two effects are balanced, leading to a relative insensitivity of dispersoid size to dpa rate. The study further shows that both coherent and incoherent dispersoids shrink during irradiation but the final equilibrium sizes of coherent dispersoids are smaller than that of incoherent dispersoids, arising primarily from a difference of their interfacial energies. Incoherent dispersoids undergo more significant volume reduction under irradiation than do coherent dispersoids.

© 2018 Elsevier B.V. All rights reserved.

1. Introduction

Oxide-dispersion-strengthened (ODS) alloys represent one class of candidate alloys with promising application in nuclear reactors due to their good creep resistance and high temperature strength [1–4]. The oxide dispersions help to stabilize grain boundaries, block dislocation motion, and act as possible defect sinks for point defect trapping and defect annihilation [2,7,8]. However, the superior performance of ODS alloys, in general, depends on the stability and structural morphologies of the dispersoids. Numerous studies have shown that under ion irradiation, dispersoids are not stable in their sizes, densities, volume fractions or chemical compositions [5,6,9–16]. Wharry and Swenson summarized a wide variety of dispersoid morphology evolution including reduced, increased, and no change in the dispersoid sizes, suggesting that multiple active mechanisms influence dispersoid irradiation

The dispersoid evolution under irradiation is governed by two competing effects: dispersoid dissolution due to damage cascade recoil and recovery arising from back-diffusion. The shrinkage of dispersoids under irradiation is described in Ref. [17]:

$$\frac{dr}{dt} = -K\psi \tag{1}$$

where r is the dispersoid radius, t is time, K is the dpa

Corresponding author.

E-mail address: lshao@tamu.edu (L. Shao).

evolution [10]. Recent studies have brought insights into the complicated nature of dispersoid stability under irradiation [11,12,14], such as cascade morphology effect and dose rate effect [11], chemical composition effect [12], and dissolution-reprecipitation mechanism [14]. Swenson et al. conducted a study comparing neutron, proton and heavy ion irradiations for the dose rate effects in dispersoid stability [11]. Their study had four orders of magnitude difference in dose rates, and the dose rate effect was coupled with different cascade morphologies [11]. Therefore, it is valuable to investigate the dose rate effect by using one single particle type, which is the motivation of the present study.

(displacements per atom) rate, ψ is a parameter to describe the efficiency of damage cascades to dissolve dispersoids. ψ is a product of l and f, where l is the thickness of a dispersoid shell which is affected by recoil damage cascades and f is the fraction of solute atoms dissolved. Hence ψ has a unit of length.

The dissolution of dispersoids leads to a concentration increase in the matrix surrounding dispersoids. Driven by a concentration gradient, back-diffusion of recoiled solutes tends to increase the dispersoid size. When these two competing effects are balanced, dispersoid sizes approach to an equilibrium value, r_e , as calculated in Ref. [18]:

$$r_e = \frac{D}{K\psi} \frac{c - c_r}{c_n - c_r} \tag{2}$$

where D is the solute diffusion coefficient influenced by radiation-induced defects, c is the solute concentration in the matrix, c_p is the solute concentration in the dispersoid, and c_r is the solubility limit at the dispersoid-matrix interface. The solubility limit at the interface is expressed as,

$$c_r = c_{\infty} \exp\left(\frac{2\gamma_i v_{at}}{kTr}\right) \tag{3}$$

where c_{∞} is the solubility for a flat interface $(r = \infty)$, γ_i is the unit interfacial energy at the dispersoid-matrix interface, v_{at} is the average atomic volume in the dispersoid, T is the temperature, and k is the Boltzmann constant [18].

Early studies did not observe a strong dose-rate dependency of dispersoid sizes [6]. According to Eq. (2), the dispersoid sizes depend on K. Hence, diffusivity D must include dose rate effects, which counterbalance dispersoid dissolution (the effect from K) and cause dispersoid diameters become insensitive to dose rate effects.

Heavy ion irradiation can induce solute redistribution and has been modelled via rate theory [19,20]. Solute migration mediated by defects produced by irradiation (i.e. vacancies and selfinterstitial atoms) was shown to result in solute gradients that, in some cases, mirror irradiation-induced defect profiles. Early studies using a focused electron beam to locally introduce damage have shown that dose rate gradients over a length scale of one micron can significantly change microchemistry due to point defect flow. The dose rate gradient effect in heavy ion irradiation, if there is any, should be detectable [20]. The sensitivities of both dispersoid dissolution and solute migration to dpa rates can be well tested in ion irradiation experiments through depth profiling of void evolution and depth dependent dispersoid characterization. Although the magnitudes of dpa rate difference are limited, the study has certain advantage of minimizing beam-heating effects, since only one beam current is used. Therefore, we utilized heavy ion irradiation in the present study to examine the oxide evolution in an Hfdoped ODS alloy. The Hf-doped alloy is specifically selected since it is extremely swelling resistant, which minimizes the complexity from dispersoid-void interactions.

2. Experimental procedure

An Hf-doped ferritic ODS alloy fabricated by Kobelco Research

Company was used in this study. The details of fabrication procedure are reported elsewhere [21]. First, the ferritic steel powder and Y_2O_3 powder are mechanically alloyed and agitated for up to 48 h under argon gas atmosphere. Then, it is degassed at high temperature in 0.1 Pa vacuum for 2 h, followed by hot extrusion at 1423 K. Hf was intentionally added for dispersoid refinement [22]. The chemical composition of this alloy is provided in Table 1. The alloy was cut into specimens of 5 mm \times 3 mm \times 2 mm, and mechanically polished down to a 0.7 mm thickness by using SiC paper (down to 4000 grit). The final polishing step used a 0.04 μ m alumina suspension. The sample was then electropolished at room temperature using a mixture of 7% perchloric acid and 93% acetic acid. The graphite cathode and the sample were biased at a voltage of 2 V and separated at a distance of 4 cm. A magnetic stirring bar was kept spinning while polishing, and the total polishing time was 20 s.

The specimen was irradiated at 475 °C by 3.5 MeV $\rm Fe^{2+}$ ions to a fluence of 9.54×10^{16} ions/cm², equivalent to 100 peak dpa. The temperature was selected since it is close to maximum swelling temperature of ferritic alloys [23–26]. The beam was static as the best practice to avoid the rastering/pulse beam effect [27]. The beam spot was about 6 mm \times 6 mm and the current was controlled to be ~200 nA. Liquid nitrogen cold traps located in the beam line and target chamber were used during irradiation to keep high vacuum (<10⁻⁸ torr). To reduce beam-induced carbon contamination, multiple beam deflectors were used to filter the carbon contaminants out of the Fe beam trajectory. Details of these instrumental setups to reduce beam contamination can be found elsewhere [28,29]. The damage calculation used Stopping and Range of Ions in Matter (SRIM) [30], with Kinchin-Pease option and an Fe displacement threshold energy of 40 eV [31].

Irradiated samples were characterized by transmission electron microscopy (TEM) with TEM specimens prepared by using the focused ion beam (FIB) lift-out technique. The FIB specimen size was $\sim 10 \, \mu m \times \sim 7 \, \mu m \times \sim 200 \, nm$ in the first-stage of preparation. Then 30 keV Ga beam was changed to 5 keV for the second-stage fine thinning to a thickness of ~100 nm. TEM characterization was performed using 200 keV FEI Tecnai G2 F20 Super-Twin and FEI Tecnai F20, and FIB was performed using Tescan Lyra-3. Bright field (BF), weak beam dark field (WBDF), scanning transmission electron microscopy (STEM) - high angle annular dark field (HAADF), high resolution TEM (HRTEM), energy dispersive spectroscopy (EDS), and electron energy loss spectroscopy (EELS) were used to characterize the samples. Dispersoid size measurement is challenging for ultra-fine dispersoids (<1 nm) due to the resolution limit of TEM. Atom probe tomography (APT) is more appropriate to characterize small dispersoids. Recent comparison studies suggest that sizes and densities of small oxide dispersoids measured by TEM and APT are comparable to each other [9]. The dispersoid sizes in the present study, although small, are still in the reliable characterization capability of TEM. Furthermore, TEM is critical for the present study in order to check coherency of dispersoids.

3. Results

Figs. 1a and b compare TEM cross-sectional micrographs before and after irradiation. In Fig. b, the upper white dashed line designates the sample surface and lower white dashed line defines the

Table 1 Composition of Hf-doped ODS alloy (wt.%).

Fe	Cr	С	Si	Mn	P	S	W	Al	Ti	Hf	Y ₂ O ₃	Ex. O
Bal	15.44	0.024	0.03	0.01	<0.005	0.002	1.80	3.90	0.12	0.59	0.33	0.10

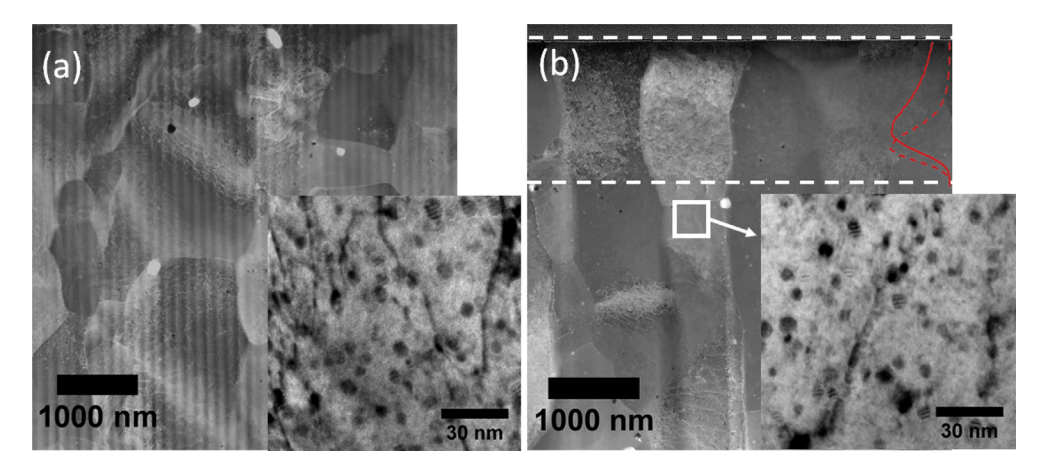


Fig. 1. STEM-HAADF and TEM BF micrographs of Hf-doped ODS alloy (a) before irradiation and (b) after 100 peak dpa irradiation. SRIM calculation of dpa (red solid line) and Fe implant (red dashed line) are superimposed in (b). Two white dashed lines in (b) refer to boundaries of the damaged region. (For interpretation of the references to colour in this figure legend, the reader is referred to the Web version of this article.)

end of the ion bombarded region. The red solid line and red dashed line superimposed on Fig. b are the dpa profile and the Fe implant profile, respectively, calculated by using the SRIM code [30]. There are no noticeable changes in grain morphologies after irradiation. The inset in Fig. 1a shows typical oxide dispersoid morphologies in the as-received condition. Dispersoid sizes in the unirradiated specimen (Fig. 1a) were measured to be 5.1 ± 0.8 nm, while the dispersoid sizes were measured to be 4.2 + 0.7 nm in the region beyond the ion range in the irradiated specimen (Fig. 1b). Hence. considering statistics, thermal annealing (corresponding to depths beyond the bombarded region) does not significantly change the dispersoid size. In both samples, there are large particles exhibiting either white contrast or dark contrast. The large particles (>100 nm) of white contrast are Hf-Ti-O, while the large particles (>50 nm) of dark contrast are Al₂O₃. Ar gas bubbles over 50 nm diameter were occasionally observed in the matrix as well. These particles and bubbles were introduced during alloy fabrication and

dpa lon distribution

Surface
250 nm

650 nm

1000 nm

1200 nm

2000 nm

2000 nm

Fig. 2. TEM bright field image of 100 peak dpa irradiated Hf-doped ODS alloy. Five different depth regions were characterized, as marked by black dashed lines. SRIM-calculated dpa and Fe ion distribution profiles are superimposed.

their densities are very low. Hence, they are not subjects of interest in the present study.

Fig. 2 shows a TEM cross-sectional micrograph of an irradiated sample, superimposed with the SRIM dpa and Fe implant profiles. The dpa peaks at a depth of ~1000 nm and the Fe implant peaks at ~1200 nm. In order to study the local dpa rate effect, five locations (as marked by black dashed lines) at depths of 250 nm (6.71 \times 10 $^{-4}$ dpa/s), 650 nm (1.19 \times 10 $^{-3}$ dpa/s), 1000 nm (1.73 \times 10 $^{-3}$ dpa/s), 1200 nm (1.06 \times 10 $^{-3}$ dpa/s), and 2000 nm (0 dpa/s) were characterized.

Dispersoids in the unirradiated sample were analyzed with EDS and HRTEM for chemical composition and structural information. HRTEM is useful to identify interfacial coherency of dispersoids and matrix. Recent studies have shown that the chemical composition of dispersoid plays an important role in the microstructure and radiation stability of the materials [11–13,32].

Fig. 3a shows a STEM-HAADF image of an oxide particle smaller than 10 nm (in an unirradiated sample). The line in Fig. 3a refers to EDS line scan across the particle. The circle and the cross refer to EDS point analyses within the particle and in the matrix, respectively. As shown in Fig. 3b, the Fe, Cr, and Al yields statistically fluctuate without a conclusive compositional variation, but Y enrichment is obvious within the particle. The two black dashed lines are used to mark where the particle starts and ends. Fig. 3c and d show two point scan results from oxide particle and matrix, respectively. Two red arrows point to yttrium signals. Yttrium appears within the dispersoid but is absent in the matrix.

Fig. 4a shows a high resolution TEM (HRTEM) micrograph of an oxide particle of ~8 nm in diameter, taken from the $[\overline{1}11]$ zone axis of the matrix. The particle has a faceted morphology, which is a sign of developing coherent interfaces. Fig. 4b shows the corresponding Fast Fourier Transform (FFT) image, with the patterns of the matrix marked with white arrows and the patterns of the particle marked with red triangles. The patterns of the particle suggest a fluorite structure of $Y_2Hf_2O_7$. The FFT pattern also shows matrix-oxide interface coherency of $(110)_{Matrix}//(\overline{2}00)_{Particle}$, and $[\overline{1}11]_{Matrix}//[011]_{Particle}$. It is reported by Dou et al. that $Y_2Hf_2O_7$ particle and bcc Fe—Cr matrix can have an orientation correlation of $(1\overline{1}0)_{Matrix}//(\overline{0}20)_{Particle}$, and $[001]_{Matrix}//[001]_{Particle}$ [33].

Fig. 5a plots the damage and Fe implant profiles, with arrows marking the regions locally characterized by TEM. Figs. 5b—f show the bright field and dark field micrographs at depths of 250 nm, 650 nm, 1000 nm, 1200 nm and 2000 nm, respectively. The above

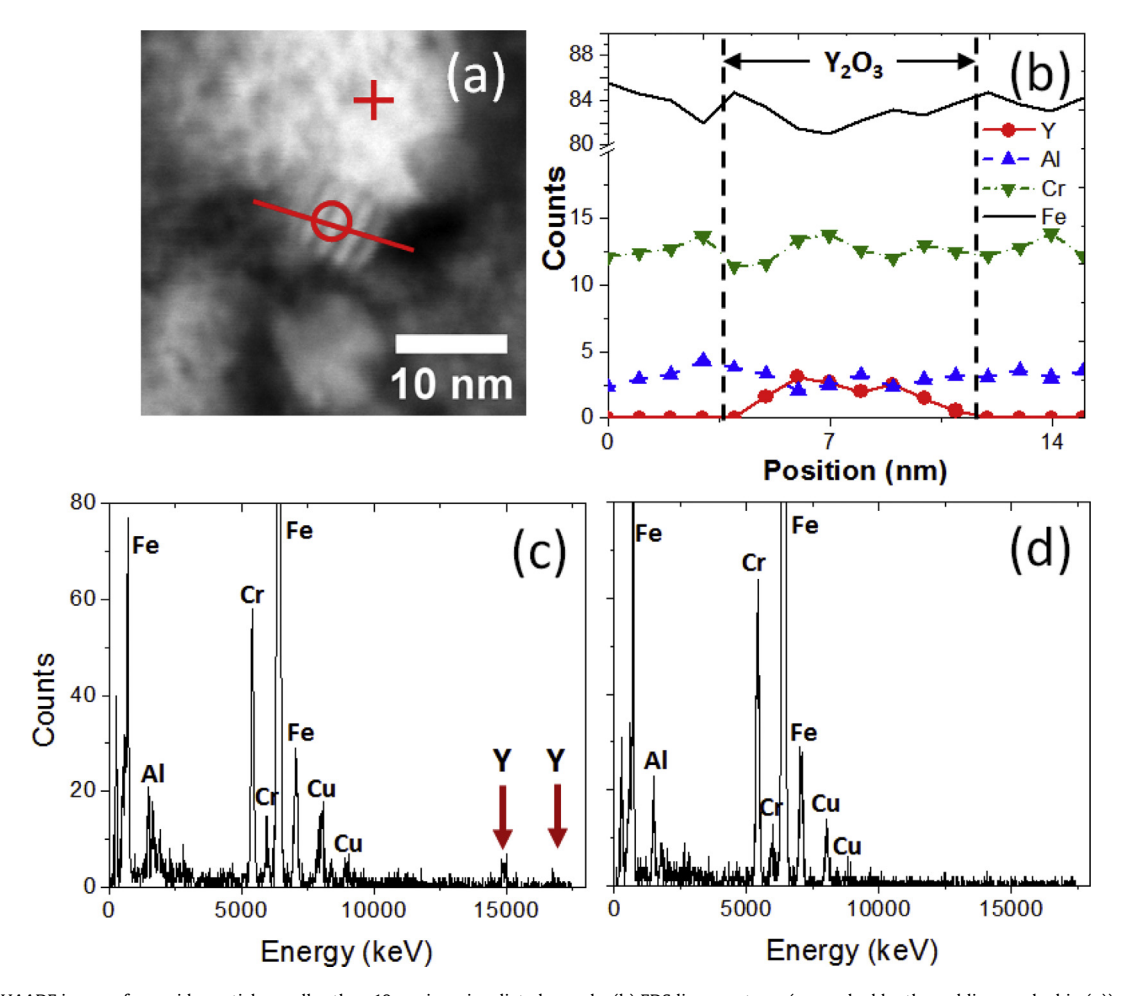


Fig. 3. (a) STEM-HAADF image of an oxide particle smaller than 10 nm in unirradiated sample, (b) EDS line spectrum (as marked by the red line marked in (a)), with two dashed lines marking the starting and ending positions of the oxide particle, (c) point spectrum obtained within the nano-oxide particle (as marked by the red circle in (a)), and (d) point spectrum from matrix (as marked by the red circle in (a)). (For interpretation of the references to colour in this figure legend, the reader is referred to the Web version of this article.)

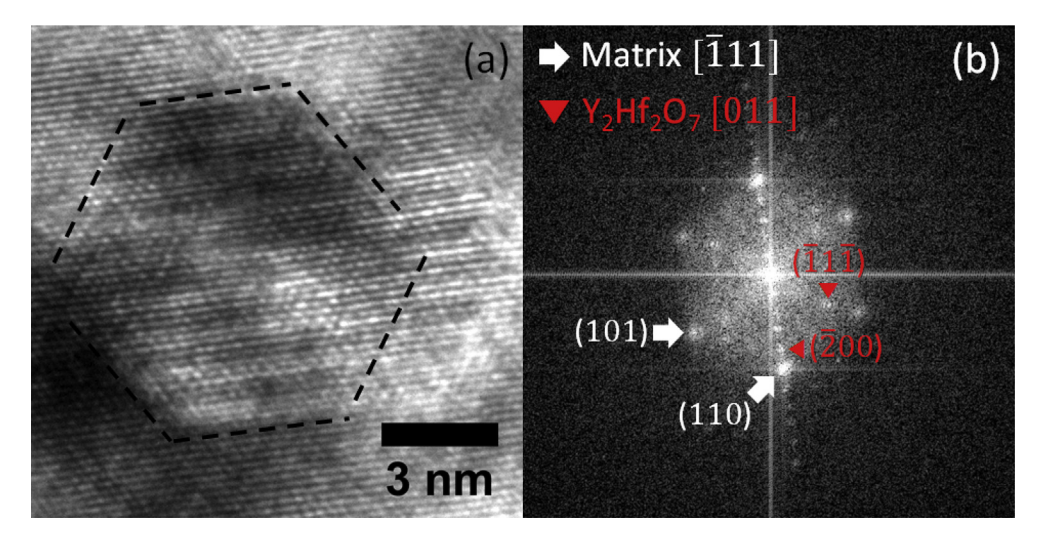


Fig. 4. (a) HRTEM image of a dispersoid in an unirradiated sample with dispersoid-matrix interfaces marked by black dashed lines and (b) the corresponding Fast Fourier Transformation (FFT) image.

depths correspond to 39 dpa (at 250 nm, 6.7×10^{-4} dpa/s), 69 dpa (at 650 nm, 1.2×10^{-3} dpa/s), 100 dpa (at 1000 nm, 1.7×10^{-3} dpa/s), 61 dpa (at 1200 nm, 1.1×10^{-3} dpa/s), and 0 dpa (at 2000 nm). The particles having dark contrast in the bright field TEM images

are oxide dispersoids. Similar to the previous studies by Chen et al. [6], when the \mathbf{g}_{110} direction is excited, dispersoids coherent to (110) of the matrix appear as bright features in the dark field images. Both dispersoid types appear dark or gray in the bright field images,

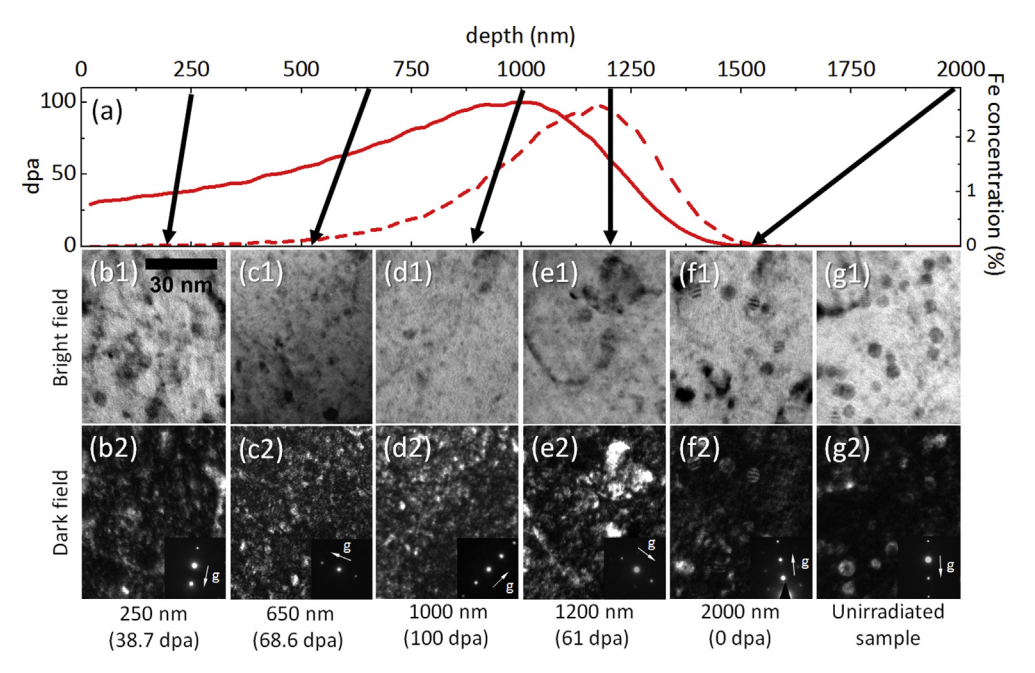


Fig. 5. (a) Dpa (red solid line) and Fe implant (red dashed line) profiles, and (b1-g1) BF micrographs at depths of 250 nm (irradiated), 650 nm (irradiated), 1200 nm (irradiated), 2000 nm (irradiated), and from unirradiated sample, and (b2-g2) corresponding WBDF micrographs and TEM diffraction patterns taken at (g, 3 g) condition with g_{110} direction excited. (For interpretation of the references to colour in this figure legend, the reader is referred to the Web version of this article.)

but only coherent dispersoids appear bright in the dark field images. Hence, the comparison between bright field and dark field images can differentiate coherent and incoherent dispersoids. Note that, as we selected one of the six (110) planes by selecting one specific \mathbf{g}_{110} direction to check the coherency, there is a possibility that some coherent dispersoids may not show up in the dark field image. However, as both coherent and incoherent dispersoid diameters are smaller than 10 nm, we assumed that all six (110) planes will develop the same coherency with the matrix, and one

dark field image taken from one specific \mathbf{g}_{110} direction can represent other five directions. For large dispersoids in Fig. 5f, they appear with Moiré fringes, suggesting a slight lattice mismatch of the dispersoid to $(110)_{\text{M}}$. These semi-coherent dispersoids also appear as bright in the dark field images. In comparison with the dispersoids at 2000 nm, which is beyond the Fe range, all dispersoids within the irradiated regions are smaller.

Figs. 6a—e summarize the detailed statistical distributions of dispersoid sizes at different depths of the irradiated sample and

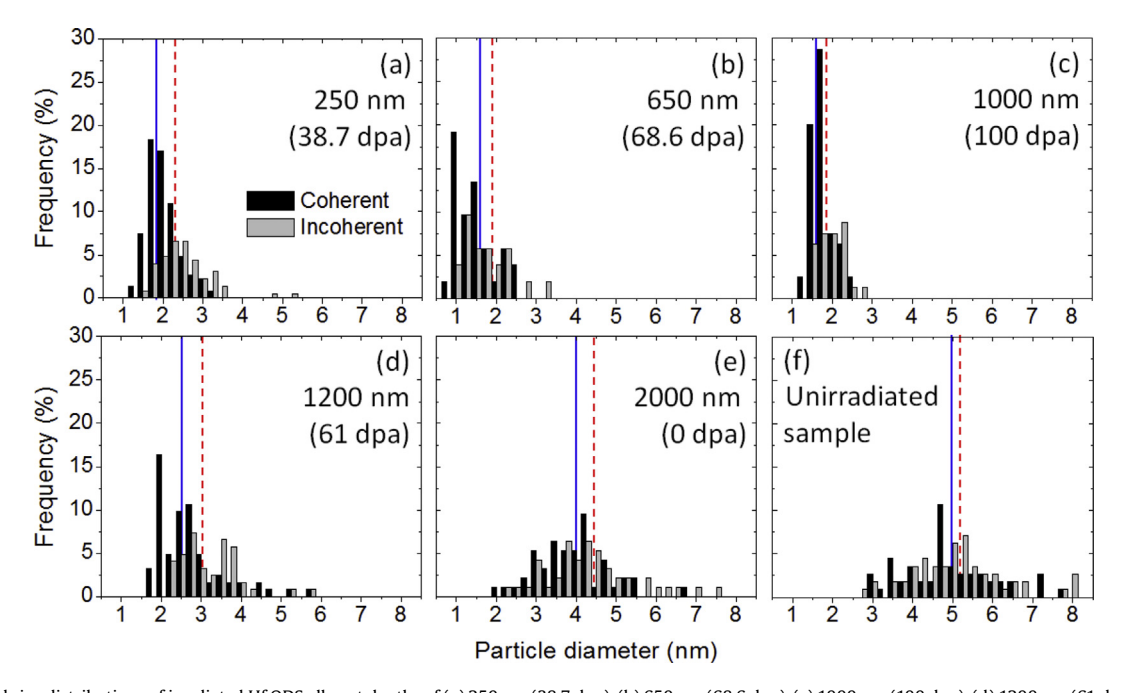


Fig. 6. Dispersoid size distributions of irradiated Hf ODS alloy at depths of (a) 250 nm (38.7 dpa), (b) 650 nm (68.6 dpa), (c) 1000 nm (100 dpa), (d) 1200 nm (61 dpa), (e) 2000 nm (0 dpa), and (f) unirradiated sample, respectively. The dark bars refer to coherent dispersoids and the gray bars refer to incoherent dispersoids. The solid blue lines and dashed red lines refer to mean diameters of coherent dispersoids and incoherent dispersoids, respectively. (For interpretation of the references to colour in this figure legend, the reader is referred to the Web version of this article.)

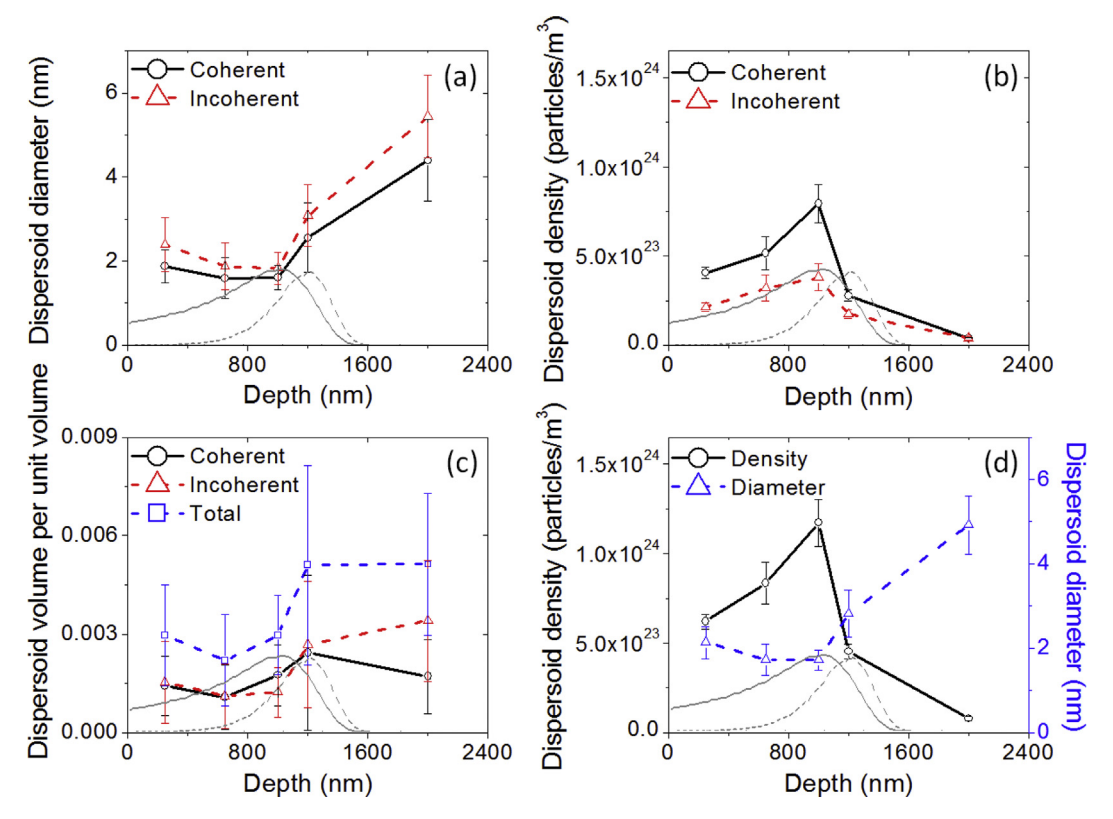


Fig. 7. Depth distributions of (a) dispersoid diameter, (b) dispersoid density, (c) dispersoid volume fraction, and (d) total dispersoid density and average diameter. Dpa (gray solid line) and Fe implant (gray dashed line) profiles are superimposed on each graph.

compare the data with that of the unirradiated sample (Fig. 6f). The dark bars refer to coherent dispersoids and the gray bars refer to incoherent dispersoids. The solid blue line refers to the mean size of coherent dispersoids and the dash red line refers to the incoherent dispersoids. In unirradiated sample, the mean sizes of coherent dispersoids and incoherent dispersoids are very close to each other. After ion irradiation, both types of dispersoids shrink. But the mean sizes of coherent dispersoids are consistently smaller than that of incoherent dispersoids.

Fig. 7a summarizes the size distributions at different depths. For each depth, more than 70 oxide particles were characterized. Although ion irradiation shrinks dispersoids, incoherent dispersoids are still statistically larger than coherent dispersoids at all depths. Within the irradiation region shallower than 1000 nm, the mean sizes of dispersoids of both types do not show obvious depth (or equivalently, dpa and dpa rate) dependencies. The mean sizes of incoherent dispersoids are 2.4 ± 0.7 nm at depth 250 nm, 1.9 ± 0.6 nm at depth 650 nm, 1.8 ± 0.4 nm at depth 1000 nm, 3.1 ± 0.7 nm at depth 1200 nm, 4.5 ± 1.2 nm at depth 2000 nm, and 5.2 ± 1.2 nm for the unirradiated sample. The mean sizes of coherent dispersoids are 1.9 ± 0.4 nm, 1.6 ± 0.5 nm, 1.6 ± 0.3 nm,

 2.6 ± 0.8 nm, 4.4 ± 1.0 nm at the corresponding depths, respectively, and 5.0 ± 1.2 nm for unirradiated sample. Table 2 lists mean, standard, skewness and kurtosis values of dispersoid size distributions.

Fig. 7b plots the dispersoid densities as a function of depth. Coherent dispersoids are systematically at higher density than incoherent dispersoids. Dispersoid densities at 250 nm and 650 nm are comparable to each other (about ~5 × 10^{23} m⁻³ for coherent dispersoids and ~3 × 10^{23} m⁻³ for incoherent dispersoids for both depths). At 1000 nm corresponding to the dpa peak, the dispersoid densities are higher (~8 × 10^{23} m⁻³ for coherent dispersoids, and ~4 × 10^{23} m⁻³ for incoherent dispersoids). The total dispersoid density at 1000 nm is about 1.5 times that at 250 nm.

Fig. 7c presents the dispersoid volume fraction. The volume fractions of coherent and incoherent dispersoids are comparable to each other within the irradiated region. For the irradiated region at depths ≤1200 nm, the total dispersoid volume fractions are systematically lower than that out of the irradiation region. The missing solute atoms can either diffuse towards the surface or be dissolved into the matrix under irradiation. Due to the fact that there is no enhancement of yttrium-rich precipitates near the

Table 2Mean, standard deviation, skewness and kurtosis values of dispersoid size distributions.

Depth		250 nm	650 nm	1000 nm	1200 nm	2000 nm	Unirradiated
Mean	Coherent	1.89	1.59	1.62	2.55	4.02	5.00
	Incoherent	2.39	1.88	1.83	3.08	4.47	5.23
Standard deviation	Coherent	0.39	0.48	0.29	0.82	0.92	1.16
	Incoherent	0.65	0.55	0.38	0.73	1.16	1.19
Skewness	Coherent	0.79	0.78	0.72	1.60	0.46	0.46
	Incoherent	1.50	1.03	0.75	1.11	0.80	0.57
Kurtosis	Coherent	0.46	-0.06	0.21	2.76	0.57	-0.07
	Incoherent	4.16	0.88	0.97	2.04	0.73	0.43

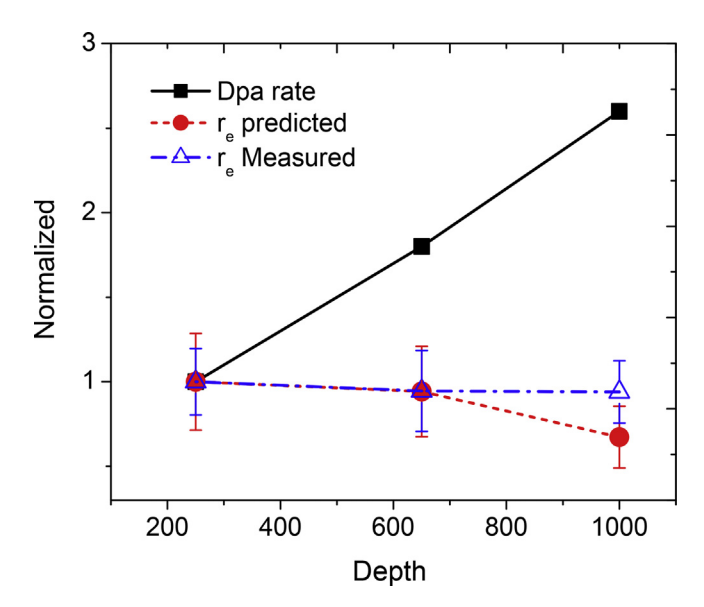


Fig. 8. Depth dependence of dpa rates, experimentally measured r_e and predicated r_e by using Eq. (7). All values are normalized to that at 250 nm.

surface, it is most likely that these solutes are dissolved in the matrix. Based on the volume fraction difference, the atomic density of dissolved solute atoms is estimated to around 0.18%. It is worth noting that, under irradiation, coherent particles undergo a much less significant volume reduction than incoherent particles do, suggesting that at the irradiation temperature of 475 °C, coherent particles are more stable than incoherent particles. This agrees with results of previous studies by Chen et al. [5,6].

As shown in Fig. 7d, total dispersoid densities within the irradiation region (at depths \leq 1200 nm) are systematically higher than that beyond the irradiated region. The total dispersoid density at 2000 nm is $7.9 \times 10^{22} \, \mathrm{m}^{-3}$, while the density at 1000 nm is $1.17 \times 10^{24} \, \mathrm{m}^{-3}$, larger by a factor of 15. The much higher dispersoid densities must result from nucleation of new dispersoids. The highest dispersoid density occurs at the dpa peak. Two possible mechanisms can contribute to this: (1) with the highest local dpa rates, the effective diffusivity of solute is peaked. Hence the likelihood of solute clustering for forming new nucleation sites is peaked, and (2) the likelihood of directly breaking large dispersoids into smaller ones is increased in the peak dpa region due to the higher density of damage cascades.

The observation that coherent dispersoids are systematically smaller than incoherent dispersoids within the irradiated region agrees with predictions of Eq. (3) in which γ_i of coherent dispersoids is smaller than that of incoherent dispersoids. The interfacial energy of coherent interfaces was reported by Ribis et al. to be $0.26-0.29\,\mathrm{J/m^2}$ [34], while the interfacial energy of incoherent or semi-coherent interfaces was reported by Howe to be $0.3-2.5\,\mathrm{J/m^2}$ energy range [35]. Using the experimentally extracted c (=0.18%) in the present study as the upper limit of c_r (since r_e in Eq. (2) must be positive), and using the estimated c ∞ (=0.013% at 475 °C) [36], we obtain the upper limit of γ_i to be about $0.4\,\mathrm{J/m^2}$ in the irradiated region and $1.0\,\mathrm{J/m^2}$ in the damage-free region in the present study.

4. Discussion

According to Eq. (2) and further assuming that D is a constant without radiation enhancement, the equilibrium dispersoid size r_e should be inversely proportional to the dpa rate K. At depths of 250 nm, 650 nm, and 1000 nm, their dpa rate ratios are 1:1.8:2.6.

Fig. 8 plots the dpa rates. In a comparison, experimentally measured r_e values are roughly constant. To explain the observations, we believe that solute diffusion must be strongly defect-assisted, as explained below.

At high temperatures in the presence of defect sinks, defect annihilation at the sinks plays a dominant role in determining defect concentrations, and therefore point defect recombination does not contribute as much. Under quasi-steady state condition, local defect reactions are governed by equations,

$$\frac{dC_V}{dt} = K - K_{VS}C_SC_V, \text{ and } \frac{dC_I}{dt} = K - K_{IS}C_SC_I,$$
 (4)

where C_V , C_I and C_S are vacancy, interstitial and sink concentrations, respectively. K_{VS} and K_{IS} are vacancy-sink reaction, and interstitial-sink reaction rate coefficients, respectively [37]. Defect populations first increase linearly with irradiation time and approach to an equilibrium steady state with constant defect concentrations expressed by,

$$C_{V_e} = \frac{K}{K_{VS}C_S}$$
, and $C_{I_e} = \frac{K}{K_{IS}C_S}$ (5)

On the other hand, for solute atoms which diffuse via interaction with point defects, a general expression of their diffusivity is given in Ref. [38]:

$$D = f_V D_V C_V + f_I D_I C_I + \dots$$
 (6)

where f is a weight factor determined by both diffusion mechanism and diffusion correlation. D_V and D_I are the diffusivities of vacancies and interstitials, respectively. The defect-assisted diffusion can extend to other defect types such as di-interstitial or divacancy. For simplicity, we ignore the mechanisms involving defect clusters.

Combining Eqs. (2), (5) and (6), we obtain

$$r_{e} = \frac{f_{V}D_{V}/K_{VS} + f_{I}D_{I}/K_{IS}}{\psi C_{S}} \frac{c - c_{r}}{c_{p} - c_{r}}$$
 (7)

Hence, there is no dependence of r_e on dpa rate K.

The defect sinks (C_S) can be dislocations, voids, or oxide dispersoids. In our irradiated samples, voids are not observed due to the good swelling resistance of the alloy matrix. Therefore, the most dominant sinks are the dispersoids themselves. As an approximation, we can use local total dispersoid density to represent C_S and calculate r_e by using Eq. (7). As shown in Fig. 8, the predicted r_e values are reasonably close to the experimentally measured values.

For Eq. (4), we assume a high temperature condition in which defect recombination contributes less in comparison with defect annihilation at sinks. Hence, interstitial-vacancy recombination is ignored. Even if this is not a high temperature condition, Eq. (4) is still valid for the case having high density defect sinks such as dispersoids in the present case. In other words, it is valid for the condition that point defects find sinks first before they find their counterpart defects for recombination [37]. For a different and extreme case in which the temperature is low and the defect sink density is also low, defect reactions are governed by the defect creation rate and interstitial-vacancy recombination only (ignoring defect-sink interaction). Then, the defect reaction equation and the quasi-steady state defect concentration are expressed as Eq. (8) [37].

$$\frac{dC}{dt} = K - K_{IV}C^{2}$$

$$C_{e}(=C_{I_{e}} = C_{V_{e}}) = \left(\frac{K}{K_{IV}}\right)^{1/2}$$
(8)

Note in this case, the defect concentrations under quasi-steady state are proportional to \sqrt{K} , instead of K. After substituting C_{ρ} into Eq. (6) for D, Eq. (2) leads to a r_e dependence on $1/\sqrt{K}$, a dependence which is quite weak. The defect concentrations under quasi-steady states of various conditions (low temperature vs. high temperature and low sink density vs. high sink density) have been systematically summarized by Was [37]. Various conditions lead to either a K dependence or \sqrt{K} dependence of quasi-steady-state defect concentrations. Regardless of the complexity arising from variations in sink density and temperature, the final r_e becomes either weakly dependent or completely independent of local dpa rates. In both cases discussed (Eqs. (5) and (8)), we assume that quasi-steady states are reached. Our previous studies show that 3.5 MeV ion irradiation of a similar ODS alloy at 475 °C leads to saturated dispersoid diameters at doses of 50 peak dpa and beyond [5,6]. Hence, we believe this assumption is valid. Otherwise, dispersoids will continue to evolve under changing defect densities.

Another significant consequence of the present study is to justify the use of ion irradiation to simulate neutron irradiation. If dispersoid sizes have weak or no dependence on dpa rates, then accelerated testing using accelerated ion irradiation can more accurately predict dispersoid evolution in reactors. However, we need to point out that the current study is limited to dpa rate differences that are less than one order of magnitude, while dpa rates in accelerator testing are typically several orders of magnitude higher than those in reactors. Hence, more systematic comparative studies involving larger dpa rates (by adjusting beam current) are needed. Furthermore, there are many other factors affecting dispersoid morphology evolution. Void swelling, for example, may change dispersoid size and density. Small voids can act as nucleation sites of dispersoids. Since we did not observe void swelling in the Hf-doped ODS in the present study, such complexity was not considered. For alloys having high density grain boundaries, such as ODS alloys prepared with extrusion and severe deformation, radiation induced grain growth or radiation induced segregation can change defect sink property, which affects dispersoid stability. Previous studies have shown that radiation induced segregation can affect both void nucleation and growth [39].

Accelerator-based heavy ion irradiation in general has complexity including, but not limited to, surface sputtering, surface defect sink effect, injected interstitials, and defect imbalance. Some effects have been recently reviewed by Zinkle and Snead [40]. Due to the fact that these effects are sensitive to detail radiation conditions, we here limit our discussions below to the condition close to the present study. For the surface sputtering effect, a recent study by Jing et al. estimated a sputtered thickness of about 14 nm by 100 peak dpa 3.5 MeV Fe ion irradiation [41], based on sputtering yield calculated from SRIM simulations. The sputtering effect and its impact on damage profile shifting, therefore, can be ignored in the present study. As for the surface defect sink effect, it is difficult to tell since the ODS alloy used in the present study is swelling resistant and we cannot observe a void depletion zone. In pure Fe, 3.5 MeV Fe ion irradiation (450 °C, 105 peak dpa) creates a 120 nm wide void depletion zone (based on the half width of the zone) [42]. Therefore, assuming defect migration is comparable in Fe and the ODS alloy, the shallowest characterization depth of 250 nm in the present study is away from the surface-affected zone. Under the combined effects of injected interstitials due to extra atoms implanted and defect imbalance due to spatial difference between interstitials and vacancies, void swelling is greatly suppressed at the Fe projected range. Under 100 peak dpa 3.5 MeV Fe ion irradiation at 450 °C, void swelling in pure Fe appears within the region from 120 nm to 825 nm. Therefore, our characterization depths of 250 nm and 650 nm are not affected by both the surface effect and the defect imbalance effect. We further believe the characterization depth of 1000 nm, corresponding to the damage peak, is also valuable for the dose rate effect studies due to the following reason. Under the defect imbalance effect, the excessive interstitials $(\Delta C = C_I - C_V)$ are peaked at about $9 \times 10^4 / \text{cm}^3$ per incident 3.5 MeV Fe ion [42]. This number is much lower than the damage peak (C_I, C_V) of $2.6 \times 10^8 / \text{cm}^3$ [42]. Void swelling is sensitive to defect imbalance (ΔC). But the defect assisted diffusion (Eq. (6)) is sensitive to defect densities (C_I, C_V) , which are orders of magnitude higher than ΔC . Therefore, the defect imbalance effect (including the injected interstitial) plays a weak role in influencing D.

5. Conclusion

A Hf-doped ferrite ODS alloy was irradiated using 3.5 MeV Fe²⁺ ion at 475 °C up to 100 peak dpa. The dispersoid coherencies, sizes and densities at different depths were characterized. Both coherent and incoherent dispersoid sizes shrunk in the ion range and the incoherent dispersoid sizes were larger than those of coherent dispersoids at all depths. The densities were increased in the ion range for both coherent and incoherent dispersoids and the coherent dispersoid densities were higher than those of incoherent dispersoids. In spite of the dpa rate differences at each depth, the dispersoid sizes do not show noticeable depth dependent changes in the experiment. To explain this, defect-assisted-diffusion mechanisms were introduced, showing that the dispersoid size has a weak or no dependence on dpa rate. Although the dpa rate differences in this study were much smaller than that between a real reactor environment and the accelerator test, the present study shows the possibility of using ion irradiation to simulate neutron irradiation for studying dispersoid stability in ODS alloys.

Acknowledgements

The research is supported by the US National Science Foundation through grant number 1708788.

References

- [1] L.K. Mansur, A.F. Rowcliffe, R.K. Nanstad, S.J. Zinkle, W.R. Corwin, R.E. Stoller, Materials needs for fusion, Generation IV fission reactors and spallation neutron sources - similarities and differences, J. Nucl. Mater. 329–333 (2004) 166–172.
- [2] G.R. Odette, M.J. Alinger, B.D. Wirth, Recent developments in irradiation-resistant steels, Annu. Rev. Mater. Res. 38 (2008) 471–503.
- [3] J. Chen, P. Jung, T. Rebac, F. Duval, T. Sauvage, Y. de Carlan, M.F. Barthe, Helium effects on creep properties of Fe-14CrWTi ODS steel at 650 °C, J. Nucl. Mater. 453 (2014) 253–258.
- [4] J. Chen, P. Jung, W. Hoffelner, H. Ullmaier, Dislocation loops and bubbles in oxide dispersion strengthened ferritic steel after helium implantation under stress, Acta Mater. 56 (2008) 250–258.
- [5] T. Chen, E. Aydogan, J.G. Gigax, D. Chen, J. Wang, X. Wang, S. Ukai, F.A. Garner, L. Shao, Microstructural changes and void swelling of a 12Cr ODS ferriticmartensitic alloy after high-dpa self-ion irradiation, J. Nucl. Mater. 467 (2015) 42–49.
- [6] T. Chen, J.G. Gigax, L. Price, D. Chen, S. Ukai, E. Aydogan, S.A. Maloy, F.A. Garner, L. Shao, Temperature dependent dispersoid stability in ionirradiated ferritic-martensitic dual-phase oxide-dispersion-strengthened alloy: coherent interfaces vs. incoherent interfaces, Acta Mater. 116 (2016) 29–42.
- [7] G.R. Odette, Recent progress in developing and qualifying nanostructured ferritic alloys for advanced fission and fusion applications, JOM (J. Min. Met. Mater. Soc.) 66 (2014) 2427–2441.
- [8] C.H. Zhang, Y.T. Yang, Y. Song, J. Chen, L.Q. Zhang, J. Jang, A. Kimura, Irradiation response of ODS ferritic steels to high-energy Ne ions at HIRFL, J. Nucl. Mater.

- 455 (2014) 61-67.
- [9] E. Aydogan, N. Almirall, G.R. Odette, S.A. Maloy, O. Anderoglu, L. Shao, J.G. Gigax, L. Price, D. Chen, T. Chen, F.A. Garner, Y. Wu, P. Wells, J.J. Lewandowski, D.T. Hoelzer, Stability of nanosized oxides in ferrite under extremely high dose self-ion irradiations, J. Nucl. Mater. 486 (2017) 86–95.
- [10] J.P. Wharry, M.J. Swenson, K.H. Yano, A review of the irradiation evolution of dispersed oxide nanoparticles in the b.c.c. Fe-Cr system: current understanding and future directions, J. Nucl. Mater. 486 (2017) 11–20.
- [11] M.J. Swenson, J.P. Wharry, Nanocluster irradiation evolution in Fe-9%Cr ODS and ferritic-martensitic alloys, J. Nucl. Mater. 496 (2017) 24—40.
- [12] X. Liu, Y. Miao, Y. Wu, S.A. Maloy, J.F. Stubbins, Stability of nanoclusters in an oxide dispersion strengthened alloy under neutron irradiation, Scripta Mater. 138 (2017) 57–61.
- [13] C.M. Parish, R.M. White, J.M. LeBeau, M.K. Miller, Response of nanostructured ferritic alloys to high-dose heavy ion irradiation, J. Nucl. Mater. 445 (2014) 251–260.
- [14] C. Lu, Z. Lu, X. Wang, R. Xie, Z. Li, M. Higgins, C. Liu, F. Gao, L. Wang, Enhanced radiation-tolerant oxide dispersion strengthened steel and its microstructure evolution under helium-implantation and heavy-ion irradiation, Sci. Rep. 7 (2017), 40343.
- [15] M.L. Lescoat, J. Ribis, Y. Chen, E.A. Marquis, E. Bordas, P. Trocellier, Y. Serruys, A. Gentils, O. Kaïtasov, Y. de Carlan, A. Legris, Radiation-induced Ostwald ripening in oxide dispersion strengthened ferritic steels irradiated at high ion dose. Acta Mater. 78 (2014) 328–340.
- [16] H. Kishimoto, R. Kasada, O. Hashitomi, A. Kimura, Stability of Y-Ti complex oxides in Fe-16Cr-0.1Ti ODS ferritic steel before and after heavy-ion irradiation, J. Nucl. Mater. 386-388 (2009) 533–536.
- [17] R.S. Nelson, J.A. Hudson, D.J. Mazey, The stability of precipitates in an irradiation environment, J. Nucl. Mater. 44 (1972) 318–330.
- [18] C. Wagner, Theory of the ageing of precipitates by redissolution (Ostwald maturing), Z. Elektrochem. 65 (1961) 581–591.
- [19] K. Vortler, M. Mamivand, L. Barnard, I. Szlufarska, F.A. Garner, D. Morgan, Simulated spatial and temporal dependence of chromium concentration in pure Fe and Fe-14%Cr under high dpa ion irradiation, J. Nucl. Mater. 479 (2016) 23–35.
- [20] T. Ezawa, E. Wakai, Radiation-induced solute segregation in Al and Ni binary alloys under HVEM irradiation, Ultramicroscopy 39 (1991) 187–196.
- [21] T. Okuda, M. Fujiwara, T. Nakai, K. Shibata, A. Kimura, M. Inoue, S. Ukai, S. Ohnuki, T. Fujisawa, F. Abe, Super ODS steels R&D for fuel cladding of next generation nuclear systems, 3) Development of high performance attrition type ball mill, in: Proc. Int. Conf. On Advanced Power Plant, Tokyo, Japan, 2009, p. 9229. May 10–14.
- [22] T. Furukawa, S. Ohtsuka, M. Inoue, T. Okuda, F. Abe, S. Ohnuki, T. Fujisawa, A. Kimura, in: Proc. Int. Conf. On Advanced Power Plant, Tokyo, Japan, 2009, p. 9221. May 10–14.
- [23] F.A. Garner, M.B. Toloczko, B.H. Sencer, Comparison of swelling and irradiation creep behavior of fcc-austenitic and bcc-ferritic/martensitic alloys at high neutron exposure, J. Nucl. Mater. 276 (2000) 123–142.
- [24] F.A. Smidt Jr., P.R. Malmberg, J.A. Sprague, J.E. Westmoreland, Swelling Behavior of Commercial Ferritic Alloys, EM-12 and HT-9, as Assessed by Heavy Ion Bombardment, STP 611, ASTM International, Philadelphia, PA, 1976, pp. 227–241.
- [25] E. Aydogan, T. Chen, J.G. Gigax, D. Chen, X. Wang, P.S. Dzhumaev,

- O.V. Emelyanova, M.G. Ganchenkova, B.A. Kalin, M. Leontiva-Smirnova, R.Z. Valiev, N.A. Enikeev, M.M. Abramova, Y. Wu, W.Y. Lo, Y. Yang, M. Short, S.A. Maloy, F.A. Garner, L. Shao, Effect of self-ion irradiation on the microstructural changes of alloy EK-181 in annealed and severely deformed condition, J. Nucl. Mater. 487 (2017) 96–104.
- [26] J.G. Gigax, T. Chen, Hyosim Kim, J. Wang, L.M. Price, E. Aydogan, S.A. Maloy, D.K. Schreiber, M.B. Toloczko, F.A. Garner, L. Shao, Radiation response of alloy T91 at damage levels up to 1000 peak dpa, J. Nucl. Mater. 482 (2016) 257–265.
- [27] J.G. Gigax, E. Aydogan, T. Chen, D. Chen, Y. Wu, W.Y. Lo, Y. Yang, F.A. Garner, The influence of beam rastering on the swelling of self-ion irradiated pure iron at 450°C, J. Nucl. Mater. 465 (2015) 343–348.
- [28] J.G. Gigax, H. Kim, E. Aydogan, F.A. Garner, S. Maloy, L. Shao, Beam-contamination-induced compositional alteration and its neutron-atypical consequences in ion simulation of neutron-induced void swelling, Mater. Res. Lett 5 (7) (2018) 478–495.
- [29] L. Shao, J.G. Gigax, D. Chen, H. Kim, F.A. Garner, J. Wang, M.B. Toloczko, Standardization of accelerator irradiation procedures for simulation of neutron induced damage in reactor structural materials, Nucl. Instrum. Meth. Phys. Res. B 409 (2017) 251–254.
- [30] J.F. Ziegler, M.D. Ziegler, J.P. Biersack, SRIM the stopping and range of ions in matter, Nucl. Instrum. Meth. Phys. Res. B 268 (2010) 1818–1823.
 [31] R.E. Stoller, M.B. Toloczko, G.S. Was, A.G. Certain, S. Dwaraknath, F.A. Garner,
- [31] R.E. Stoller, M.B. Toloczko, G.S. Was, A.G. Certain, S. Dwaraknath, F.A. Garner, On the use of SRIM for computing radiation damage exposure, Nucl. Instrum. Meth. Phys. Res. B 310 (2013) 75–80.
- [32] C. Lu, Z. Lu, R. Xie, Z. Li, C. Liu, L. Wang, Effect of Y/Ti atomic ratio on microstructure of oxide dispersion strengthened alloys, Mater. Char. 134 (2017) 35–40.
- [33] P. Dou, A. Kimura, R. Kasada, T. Okuda, M. Inoue, S. Ukai, S. Ohnuki, T. Fujisawa, F. Abe, S. Jiang, Z. Yang, TEM and HRTEM study of oxide particles in an Al-alloyed high-Cr oxide dispersion strengthened ferritic steel with Hf addition, J. Nucl. Mater. 485 (2017) 189–201.
- [34] J. Ribis, Y. de Carlan, Interfacial strained structure and orientation relationships of the nanosized oxide particles deduced from elasticity-driven morphology in oxide dispersion strengthened materials, Acta Mater. 60 (2012) 238–252.
- [35] J.M. Howe, Interfaces in Materials, Wiley-Interscience, 1997.
- [36] H. Okamoto, J. Phase Equil. 16 (1995), 473-473.
- [37] G.S. Was, Fundamentals of Radiation Materials Science: Metals and Alloys, Springer, 2007, p. 218.
- [38] M. Nastasi, J. Mayer, J.K. Hirvonen, Ion-solid Interactions: Fundamentals and Applications, Cambridge University Press, New York, 1996.
- [39] W.G. Wolfer, L.K. Mansur, J. Nucl. Mater. 91 (1980) 265.
- [40] S.J. Zinkle, L.L. Snead, Opportunities and limitations for ion beams in radiation effects studies: bridging critical gaps between charged particle and neutron irradiations, Scripta Mater. 143 (2018) 154–160.
- [41] J. Wang, M.B. Toloczko, N. Bailey, F.A. Garner, J. Gigax, L. Shao, Modification of SRIM-calculated dose and injected ion profiles due to sputtering, injected ion buildup and void swelling, Nucl. Instrum. Meth. Phys. Res. B 387 (2016) 20–28
- [42] L. Shao, C.C. Wei, J. Gigax, A. Aitkaliyeva, D. Chen, B.H. Sencer, F.A. Garner, Effect of defect imbalance on void swelling distributions produced in pure iron irradiated with 3.5 MeV self-ions, J. Nucl. Mater. 453 (2014) 176–181.